Effects of Cooling Rate on the Microstructure and Tensile Properties of Powder Metallurgy Ti$_2$AlNb Alloy

XIAOSHENG TIAN,[1,2] JIE WU,[1] ZHENGGUAN LU,[1] RUIPENG GUO,[3] LEI XU,[1,4] and RUI YANG[1]

1.—Shi-changxu Innovation Center for Advanced Materials, Institute of Metal Research, Chinese Academy of Sciences, Shenyang 110016, China. 2.—School of Materials Science and Engineering, University of Science and Technology of China, Shenyang 110016, China. 3.—College of Materials Science and Engineering, Taiyuan University of Technology, Taiyuan 030024, China. 4.—e-mail: lxu@imr.ac.cn

The effect of cooling rate on the microstructure and tensile properties of powder metallurgy (PM) Ti$_2$AlNb alloy was studied. The Ti$_2$AlNb pre-alloyed powder was produced by electrode induction melting gas atomization (EIGA) and then fabricated by hot isostatic pressing (HIP) at 1030°C with applied pressure of 130 MPa, holding for 3 h. All samples were solution treated at 980°C for 2 h, cooled at different cooling rates. The results showed that, with increasing cooling rate, the tensile strength increased to a maximum value and then decreased. The multiphase structure consists of dispersive α$_2$ phase, O phase and B2 phase matrix by furnace cooling (including four different cooling rates). At these cooling rates, all alloys have excellent elongation at room temperature (RT) and 650°C. Under air cooling and water cooling, only α$_2$ and B2 phase exist in these alloys, and they have better elongation at room temperature. At 650°C, a sharp drop in plasticity has been obtained because of the fine acicular O phase precipitates, which will reduce the resistance of crack propagation along the prior B2 grain boundary.

INTRODUCTION

Ti$_2$AlNb alloys have been potential structural materials for aircraft engine applications since 1988 because of their high specific strength and excellent oxidation and creep resistance at elevated temperature.[1–3] However, elemental inhomogeneity is a key problem with Ti$_2$AlNb alloys formed by traditional process due to the difference in the aspects of melting point, density and diffusion coefficient of the main constituent elements: Ti, Al and Nb.[4] Powder metallurgy, among several competing mass production methods, plays an important role not only as a means of saving material and energy but also as a technique that fabricates materials with uniform microstructure. Several endeavors have been devoted to producing PM Ti$_2$AlNb alloys by vacuum hot pressing (HP),[5] spark plasma sintering (SPS) technique[6,7] as well as HIP using pre-alloyed powder.[8,9] Near net shape forming is a technology that requires only a small amount of processing or no longer processing of shaped parts. Xu et al.[10,11] carried out a series of studies and successfully prepared PM Ti$_2$AlNb complex components.

The mechanical properties of Ti$_2$AlNb alloys are sensitive to phase composition and microstructure. Therefore, extensive studies are required on the microstructure's accurate control of these properties. Heat treatment is an important means to control the stability of microstructure. Many studies have been carried out on the heat treatment system, microstructure and mechanical properties of Ti$_2$AlNb alloys.[12–17] These results have shown that the mechanical properties of Ti$_2$AlNb alloys depend on the microstructure, and the phase balance and microstructure evolution are very complicated. Under different heat treatments, Ti$_2$AlNb alloys have a single-, two- or three-phase structure. In

addition, the size, volume fraction and morphology of these phases will also have a great influence on the mechanical properties. During the cooling process, large complex components will cause differences in their microstructure and mechanical properties due to their different size.[18] Hence, it is necessary to study the effect of cooling rate on the microstructure and mechanical properties of alloys. Luo et al.[19] through the study of Ti-22Al-21Nb-1Ta-1W (at%) alloy showed that as the cooling rate increases, the yield strength first decreases and then increases, and the change in elongation has an opposite trend to the yield strength. According to the cooling rate study of Ti-22Al-24Nb-0.5Mo (at%) alloy by Zhao et al.,[20] the four cooling rates of furnace cooling, air cooling, oil quenching and water quenching have an effect on the microstructure and tensile properties. The results show that with the increase of the cooling rate, the tensile strength at 650°C gradually increases, and the strength and plasticity at RT also tend to increase. The above research mainly focuses on forging Ti$_2$AlNb alloy, and there is little research on PM Ti$_2$AlNb alloy. Li et al.[21] only studied the effects of water quenching and furnace cooling on PM Ti-22Al-25Nb (at%) alloy. With the engineering application of PM Ti$_2$AlNb alloy, it is necessary to study the influence of different cooling rates on the alloy in detail.

In this study, the EIGA pre-alloyed powder of Ti-22Al-24Nb-0.5Mo (at%) alloy was prepared PM Ti$_2$AlNb alloys by HIP. Microstructural evolution and tensile properties at RT and 650°C were investigated systematically under different cooling rates. It is expected to build the relation among the phase composition, microstructure, mechanical properties and cooling rates.

MATERIALS AND METHODS

The pre-alloyed powder of Ti-22Al-24Nb-0.5Mo (at%) was produced by EIGA. Figure 1a shows surface morphologies and microstructures of the EIGA Ti$_2$AlNb pre-alloyed powder. The powders were in general spherical in shape and had a smooth surface; only a few had attached satellites. Besides, the dendritic surface morphologies can be observed on the coarse powder surface. The powder with a normal size distribution was measured by using a Mastersizer 2000 laser size analyzer. The average particle size was about 100 μm. The particle size distribution of the powder basically conforms to the normal distribution. The powder filling, degassing treatment and sealing have been introduced in detail in previous studies.[22,23] The alloys were prepared by HIP at 1030°C with applied pressure of 130 MPa, holding for 3 h. Figure 1b displays the microstructures of PM Ti$_2$AlNb alloy before heat treatment. There are no pores in the microstructure of PM Ti$_2$AlNb alloy, indicating that the alloys achieve full densification. Xu et al.[10] prepared a fully dense Ti$_2$AlNb alloy without prior particle boundaries using the same hot isostatic pressing process. The alloy is mainly composed of equiaxed α_2 phase, lath O phase and B2 matrix. Equiaxed α_2 phase is distributed at or near grain boundaries, and lath O phase is evenly distributed in B2 matrix. In previous work,[24] the as-HIPed Ti$_2$AlNb alloy microstructure generally consists of three phases, equiaxed α_2 phase and lamellar O + B2 phases inside the grain.

The specimens were heat treated at 980°C for 2 h[25] and then cooled with different cooling rates, as shown in Fig. 2. The average cooling rates from 980°C to 600°C for different cooling methods are shown in Table I.

As-received materials were machined into dogbone type specimens with a diameter of 10 mm and a gage length of 25 mm. The samples had been tested at RT on an electronic universal testing machine (CMT5305) and at 650°C on an SDGL 300/1100 machine. The tests were conducted under strain control mode with a strain rate of 1.5 mm/min. The samples were cut from the vicinity of the tensile fracture and then ground, polished and chemically etched. The phase composition and the microstructure of the alloys with different cooling rates were then characterized by x-ray diffraction
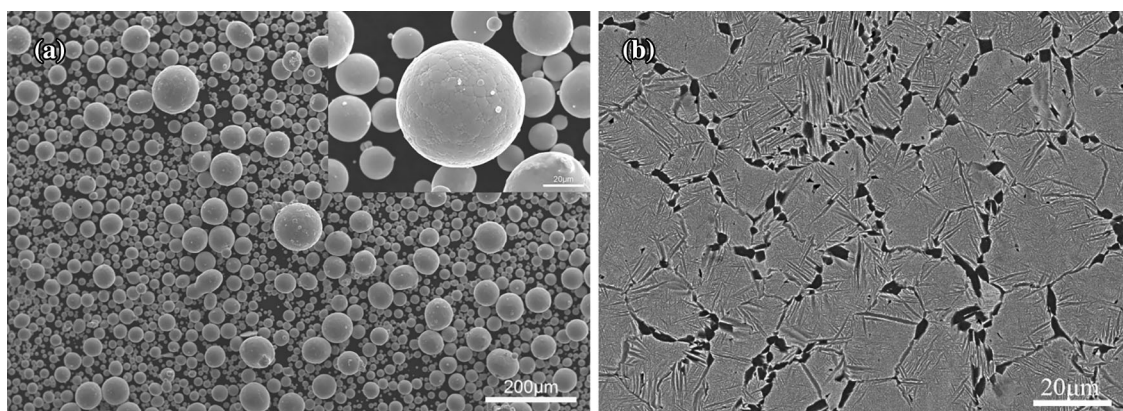

Fig. 1. Morphologies of Ti$_2$AlNb powder (a) and high-magnification of the upper right corner and microstructures of powder metallurgy Ti$_2$AlNb alloy before heat treatment (b).

(XRD, D/MAX 2400 with Cu Kα radiation at a scanning speed of 10°/min) and scanning electron microscopy (SEM, TESCAN NIRA3), respectively. The etched agent consisted of 5% HF, 10% nitric acid and 85% deionized water (by volume). The volume fraction and the average width of α_2, B2 and O phases in SEM images of samples with different cooling rates were measured and quantitatively analyzed by Image-Pro Plus 6.0 software. TEM images were obtained using a FEI Talos F200X operated at 120 kV. TEM samples were prepared by standard mechanical polishing and ion thinning.

RESULTS

Phase Constituents of Ti₂ AlNb Alloys with Different Cooling Rates

Figure 3 shows the XRD patterns of the samples with different cooling rates. The phase constitutions of the tensile samples at RT are shown in Fig. 3a. There is no single diffraction peak of O phase in air cooling (C5) and water cooling (C6) samples, as shown in the red dotted lines (25° and 42°) in Fig. 3a. Therefore, it is impossible to confirm the existence of O phase in these two states, and further study is needed. The critical rate for the complete depression of O phase precipitation is 4°C/s.[26] The absence of O phase is mainly due to the C5 and C6 cooling rates > 4°C/s. Figure 3b shows the XRD

Fig. 2. Different heat treatment methods.

patterns of the tensile samples at 650°C. All samples contain B2, α_2 and O phase. Compared with the tensile samples at RT, the single diffraction peaks of O phase (25° and 42°) also appear in air cooling (C5) and water cooling (C6). The results show that O phase is precipitated in the tensile test at 650°C. The experimental results and previous work[21] reveal that the fine O phase lathes will be precipitated during tensile test at 650°C after solution treatment at 980°C.

The modified Ti₂AlNb alloy's B2 phase peak shifted to a higher angle than the Ti₂AlNb alloy's (111) peak, while the O phase peak positions stayed the same. In the B2 phase, a stabilizing element (Mo) replaces Nb atoms, reducing cell volume because of the smaller atomic radius of Nb. This can be attributed to this occurrence. As a result, the B2 phase's (041) face interplanar spacing should be lowered. Furthermore, the B2 peak's displacement rose as the cooling rate/time increased, which showed that the amount of Nb atoms entering the B2 lattice during heating was growing.

Microstructure of Ti₂ AlNb Alloys with Different Cooling Rates

The cross-sectional microstructure of the tensile samples at room temperature and 650°C is shown in Fig. 4. The microstructure with resistance furnace cooling (C1) is depicted in Fig. 4a and b, which is mainly composed of equiaxed α_2 phase, lath O phase and B2 matrix. Equiaxed α_2 phase is distributed at or near grain boundaries, and lath O phase is evenly distributed in B2 matrix. There is no obvious change in the microstructure between RT and 650°C. The microstructure with vacuum furnace cooling (C3) and resistance furnace cooling (C1) is similar, as shown in Fig. 4c and d. However, the size of the O phase is different in the two cooling rates. At room temperature, the average width of O phase is 270 nm at C1 cooling rate and that of C3 is 120 nm. After holding at 650°C for 20 min, the average width of O phase decreases, which is mainly due to the fine O phase precipitated at 650°C, resulting in the decrease of the overall average width. Figure 4e and f shows that the microstructure of RT tensile and 650°C tensile with water cooling (C6) is obviously different. With water cooling (C6), the microstructure of the tensile sample at RT only consists of α_2
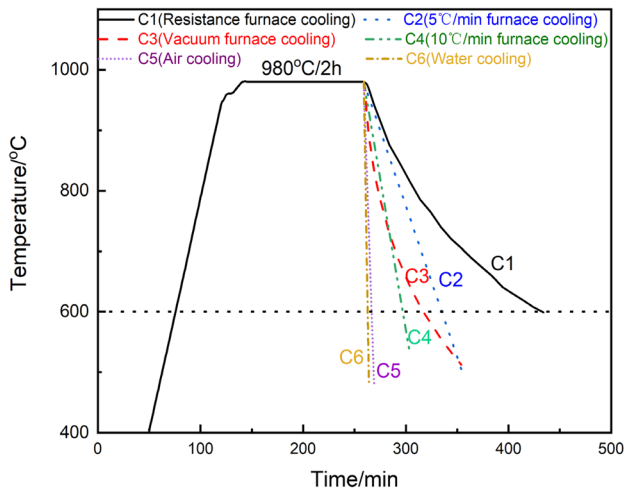
Table I. Different heat treatment cooling rates

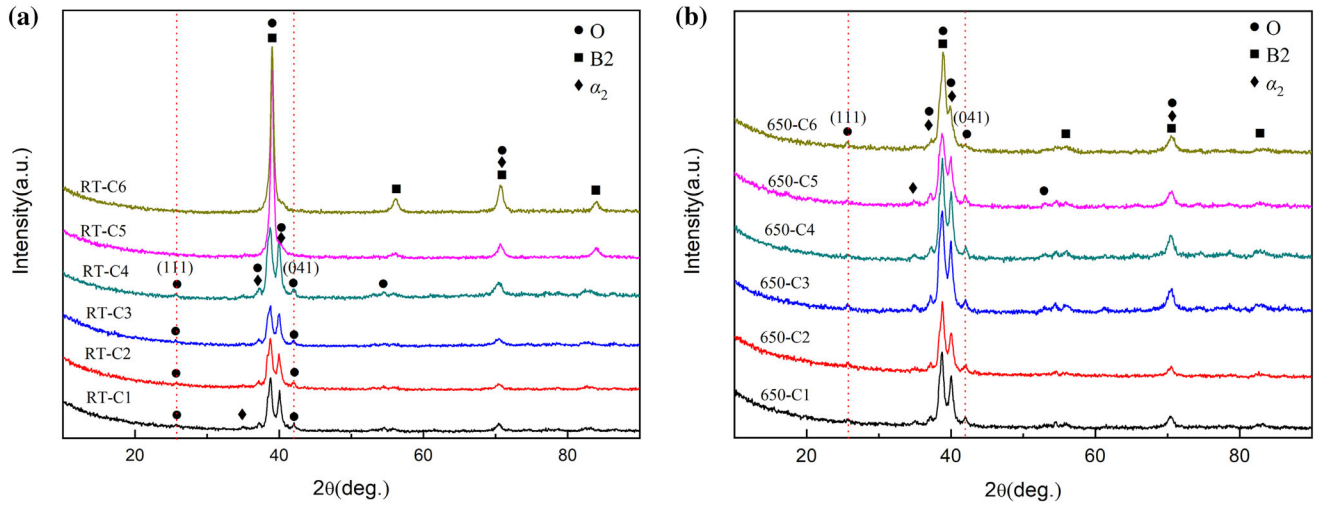| Symbol	Cooling methods	Average cooling rate range
C1	Resistance furnace cooling	2.18°C/min
C2	5°C/min furnace cooling	5°C /min
C3	Vacuum furnace cooling	4.93°C /min
C4	10°C/min furnace cooling	10°C /min
C5	Air cooling	> 500°C /min
C6	Water cooling	> 1.2×10^4°C /min[27]

Fig. 3. XRD patterns of Ti$_2$AlNb alloy with different cooling rates at (a) RT and (b) 650°C.
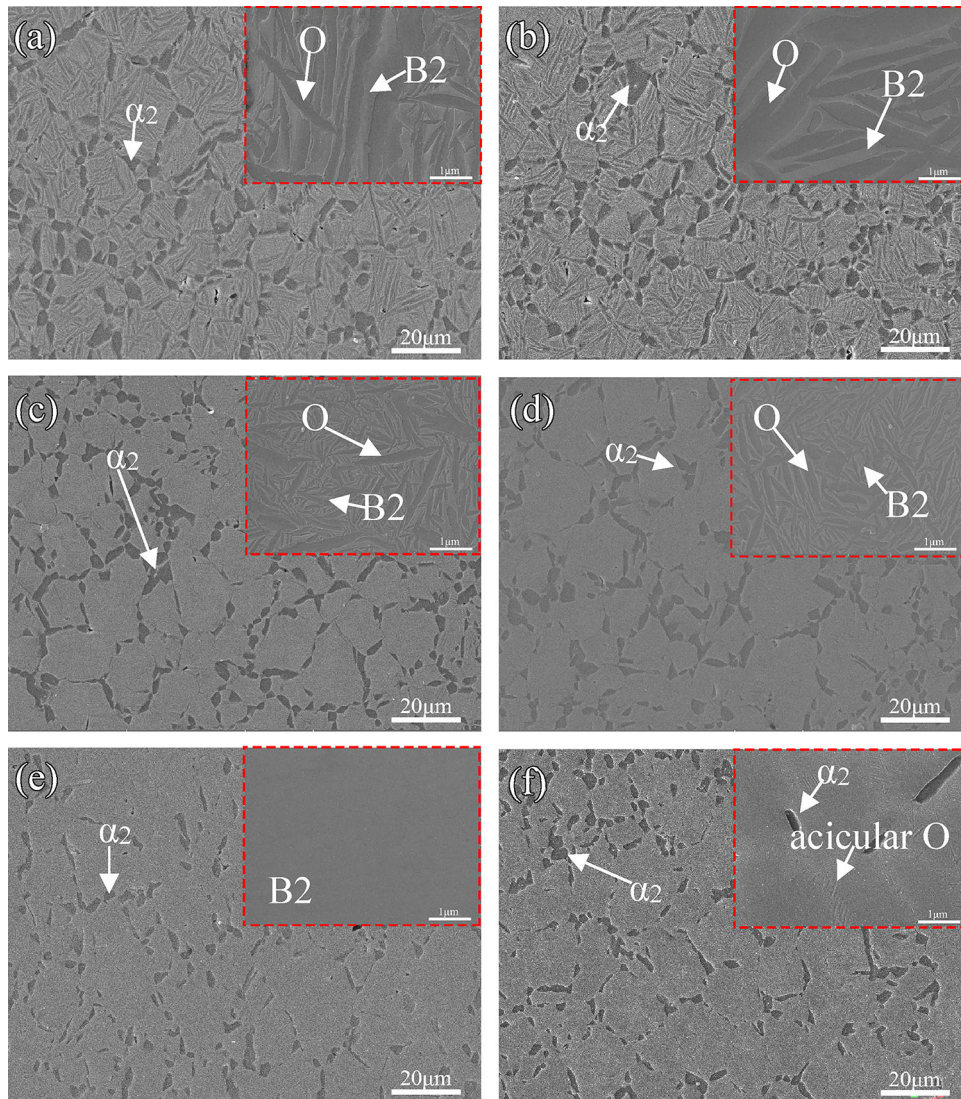

Fig. 4. Microstructure at RT and 650°C: (a), (b) resistance furnace cooling, (c), (d) vacuum furnace cooling, (e), (f) water cooling.

phase and B2 matrix, as shown in Fig. 4e. The O phase disappeared because of rapid cooling after solution treatment. Many acicular O phase particles precipitated from the B2 phase, as reported by previous work[3,23]. After holding at 650°C for 20 min, the average width of O phase is 40 nm at C6 cooling rates in Fig. 4f.

Figure 5 depicts the TEM images taken from the samples with different cooling rates then holding at 650°C for 20 min. Figure 5a shows the TEM bright-field image of the sample with resistance furnace cooling. Numerous O phases were uniformly distributed inside the B2 phase matrix. A small amount of ultrafine acicular O phase was also
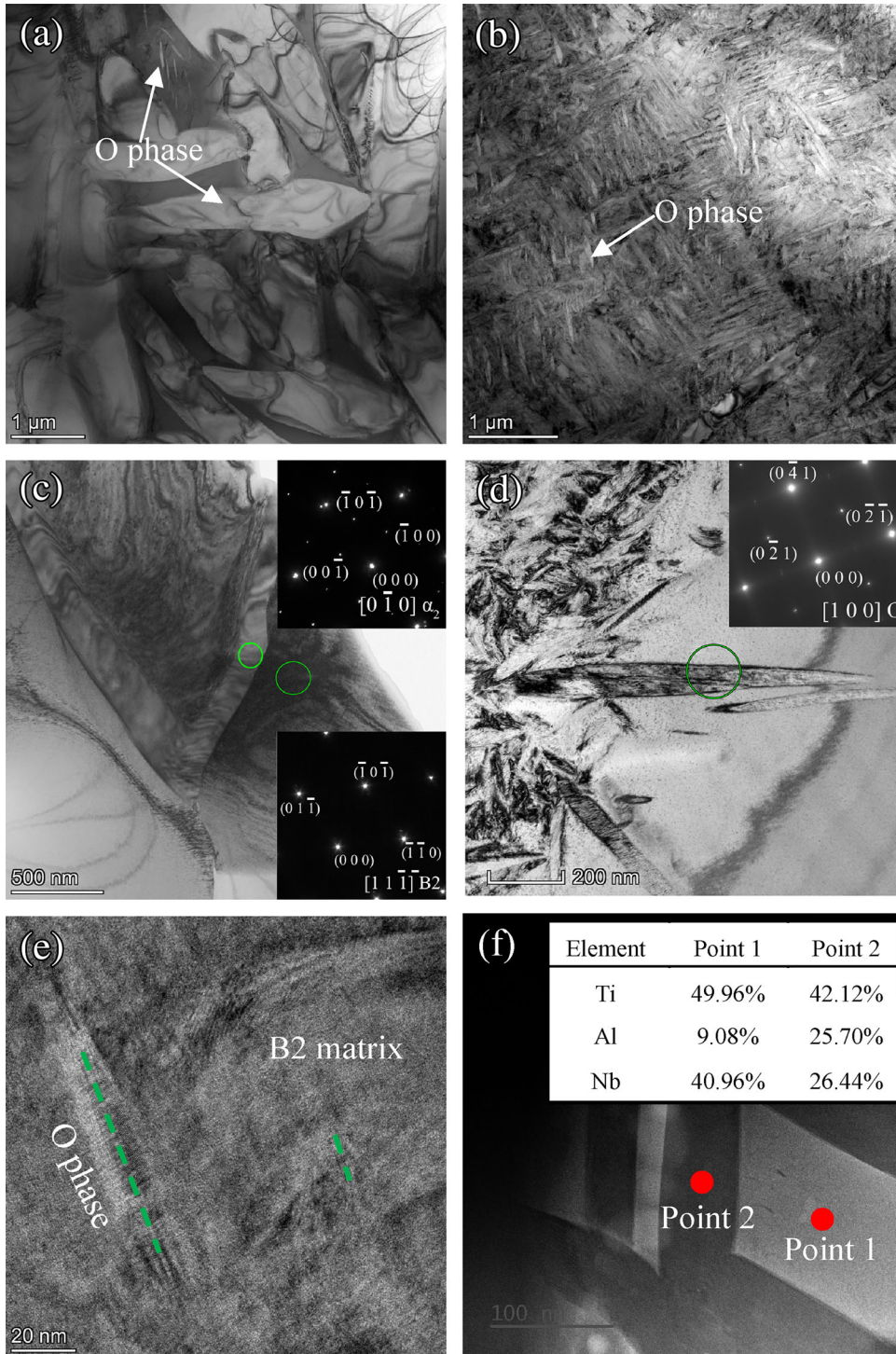

Fig. 5. TEM images of the samples with different cooling rates then holding at 650°C for 20 min: (a) resistance furnace cooling; (b), (c), (d), (e), (f) water cooling.

precipitated in the B2 matrix. As shown in Fig. 5b, after holding at 650°C for 20 min, numerous ultrafine O phases precipitate in the B2 phases grain boundary and interior. Figure 5c shows the TEM micrograph of water-cooling samples and electron diffraction patterns of α_2 and B2 phases. It is proved again that there are only α_2 and B2 phases and no O phase in the tensile samples with water cooling at RT. The results revealed that the ultrafine acicular O phase precipitated at 650°C, as mentioned in Figs. 3 and 4. Figure 5e shows the HRTEM image taken from the sample with C6. The size of the two O phases is less than a dozen nanometers. The results confirmed the phase transformation mechanism of B2 $\rightarrow$ O.[5,7,27] The EDS results show that the gray phase (point 1) consists of 49.96% Ti, 9.08% Al and 40.96% Nb (at) and the dark phase of 42.12% Ti, 25.70% Al and 26.44% Nb (at). Such results show that these dark phases are O phases.

Mechanical Properties

Tensile Properties

The RT and 650°C ultimate tensile properties of the samples with different cooling rates are presented in Fig. 6. Representative stress-strain curves with different cooling rates at room temperature are shown in Fig. 6a. Here the true strain was calculated from the extensometer reading. The sample with C5 and C6 exhibited no work hardening, while the samples with C1–C4 showed a little work-hardening effect. Figure 6b shows the strength and ductility of the samples at RT. With the increase of cooling rate, the RT ultimate tensile strength and yield strength of the alloys first increase and then decrease. When the alloy is cooled with vacuum furnace cooling (C3), the ultimate tensile strength and yield strength reach the maximum value of 1239 ± 6 MPa and 1052 ± 6 MPa, respectively. However, it has the lowest elongation of 11.2 ± 1.6%. Compared with C1–C4, the elongation of air cooling (C5) and water cooling (C6) is 16.7 ± 0.6% and 16.5 ± 0.5%, respectively.

As shown in Fig. 6c, while the elongation decreased from C1 to C6, the change trend of ultimate tensile strength and yield strength at 650°C is consistent with that at RT. The sample with C3 exhibited the largest ultimate tensile strength and yield strength value, which are 935 ± 6 MPa and 792 ± 2 MPa, respectively. The elongation remained nearly constant between RT and 650°C. A severe drop in elongation was observed at 650°C for the samples with C5 and C6, but the phenomenon was absent in the samples with C1–C4. The elongation of the alloys with air cooling (C5) and water cooling (C6) is only 1.8 ± 1.8% and 3.7 ± 3.1%, respectively.

Fracture Characteristics

Figure 7 shows the tensile fracture morphology of PM Ti₂AlNb alloy at RT and 650°C. The fracture morphologies of tensile samples with resistance furnace cooling (C1) are shown in Fig. 7a and b. Some dimples with different sizes and depths are observed. The fracture mechanism is ductile fracture at both RT and 650°C. The microscopic fracture morphology shown in Fig. 7c has a similar morphology to that of the samples with C1, which also indicates a ductile fracture mode. The samples exhibited ductile fracture at RT but a small portion of cleavage fracture was also recognized for the sample with C3 at 650°C (Fig. 7d). Ductile dimples were evident throughout the fracture surfaces of samples tested at RT in Fig. 7e. Obvious plastic deformation was identified in the samples with C5 at room temperature, which corresponded to the large elongation. Therefore, there were some big cracks at the center of the sample and some dimples near the cracks (as shown by the white arrow). Fracture morphology of 650°C tensile samples with water cooling is shown in Fig. 7f. The fracture surface is characterized by brittle fracture, an obvious crystal sugar pattern and typical intergranular fracture. Several cracks formed by the fracture of the B2 phase grain boundaries can be clearly recognized. Slip bands were present at some facets, while at other facets there were only very smooth surfaces and no slip bands could be observed.

DISCUSSION

The alloy is mainly composed of equiaxed α_2 phase, lath O phase and B2 matrix before heat treatment. As previously reported in the literature, the DSC thermograms of Ti₂AlNb pre-alloyed powder heating from 150°C to 1200°C were given.[8] Heat treatment temperatures were selected to be 980°C, which is B2 + α_2 + O phase region. However, the temperature is closer to α_2 + O phase region. Lamellar O phases precipitate from B2 grains during the slow cooling process from B2 + α_2 + O phase region to room temperature. Contrarily, there are only two phases of B2 + α_2 in the samples during the faster cooling process (air cooling and water cooling). The test temperature is 650°C, which is slightly higher than the transition temperature $T_{O \rightarrow O + B2}$. The samples were held at 650°C for about 20 min during testing, and a large amount of fine O phase particles were precipitated from B2 phase, as reported by other workers.[3]

The size and volume fraction of O phases have a significant effect on the mechanical properties of the PM Ti₂AlNb alloys. The volume fraction and size of phases at RT and 650°C with different cooling rates were calculated by Image-Pro Plus 6.0 software. The results are shown in Fig. 8. At room temperature, the volume fraction of O, B2 and α_2 phase is similar at different cooling rates of C1–C4. The width of lamellar O is 270–120 nm from C1 to C4. For RT
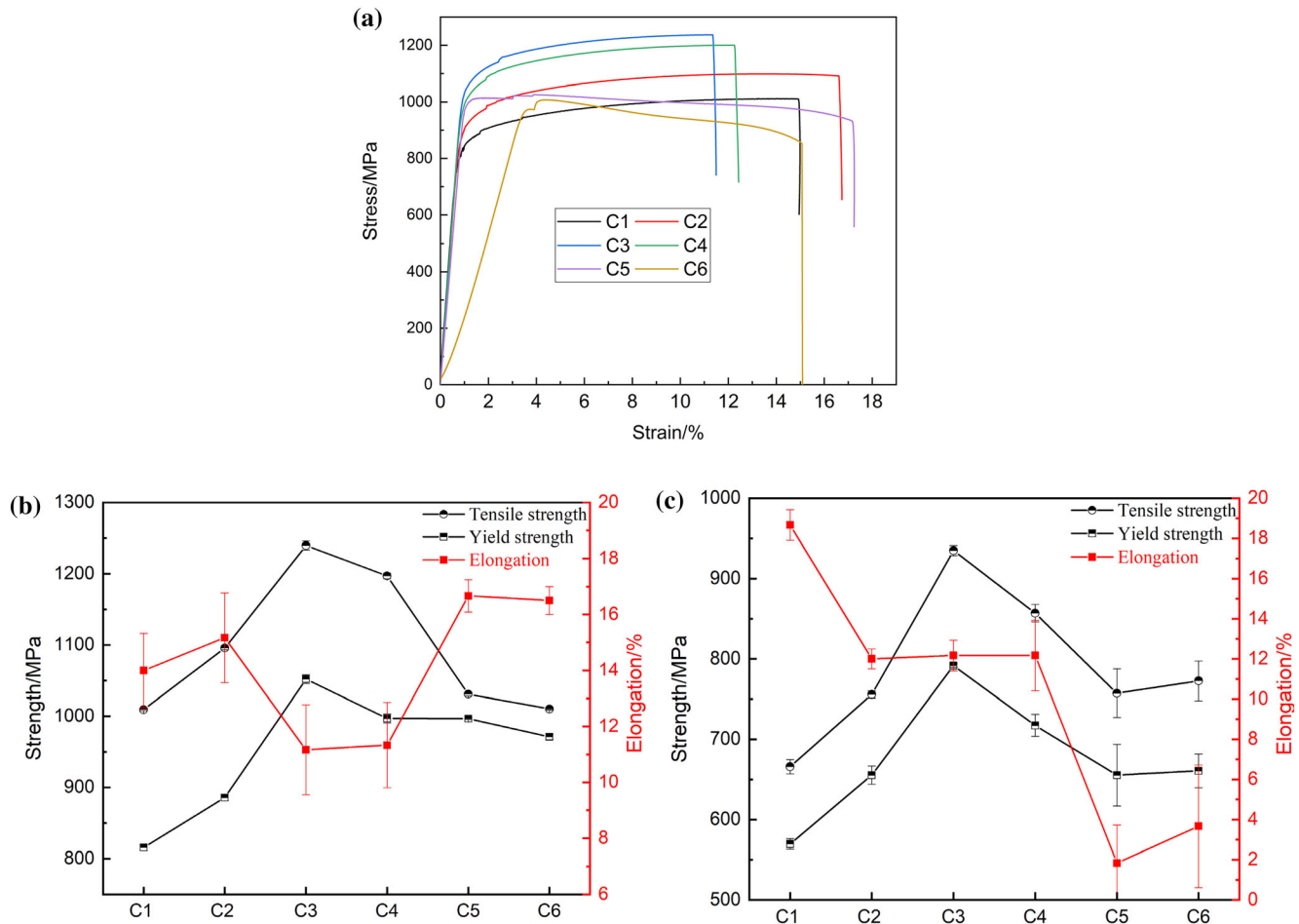
Fig. 6. Stress-strain curves of (a) RT, tensile properties of the samples with different cooling rates at (b) RT and (c) 650°C.

samples, from C1 to C3, the ultimate tensile strength increased by approximately 200 MPa and the elongation dropped by approximately 4% (Fig. 6-a). According to the Hall-Patch relationship,[28] smaller grains are always beneficial to the strength of the alloys. Wei et al.[29] found that the coarse lamellar O phase can improve the ductility of alloys. Therefore, the maximum ultimate tensile strength and minimum elongation are obtained for C3. The alloy with C1–C4 is α_2 + O + B2 microstructure, and the alloy with C5–C6 is α_2 + B2 microstructure. The slip compatibility between O and B2 phases and the strengthening of the B2-dominated microstructure by the O phase give the α_2 + O + B2 microstructure an optimal balance between strength and ductility.[3,30,31]

The samples with α_2 + B2 microstructure had the greatest elongation at room temperature. B2 phase is the matrix phase, and it has a body-centered cubic structure. B2 phase has many slip systems, and thus it has excellent ductility.[6] This phase is beneficial to improve the elongation of the alloy, so the samples with air cooling and water cooling have a higher elongation. This result is consistent with

other studies, showing that the presence of the B2 phase is beneficial to improve the plasticity of the alloy.[2,30]

The elongation of samples with α_2 + B2 microstructure appeared to have an elongation maximum at room temperature (16.7 ± 0.6%), and it dropped by nearly 80% at 650°C. The microstructure of the samples changed from α_2 + B2 to α_2 + B2 + O. However, compared to the samples with C1–C4, the volume fraction and size of O phase are small. The average width of O phase is 60 nm and 40 nm, respectively.

When the sample is tested at 650°C, a large amount of fine O phase precipitates out of the B2 phase, resulting in a decrease in the plasticity of the sample.[3,32,33] Fine O phase has high strength and difficult deformation. The plastic deformation in tension is mainly provided by B2 phase, which leads to the incongruity of deformation of O phase and B2 phase. The cracks initiate at the interface between O phase and B2 phase and propagate along the interface, resulting in premature fracture of the sample. Under this condition, the tensile sample always has small plastic deformation after fracture. However, the O phase volume fraction of the sample
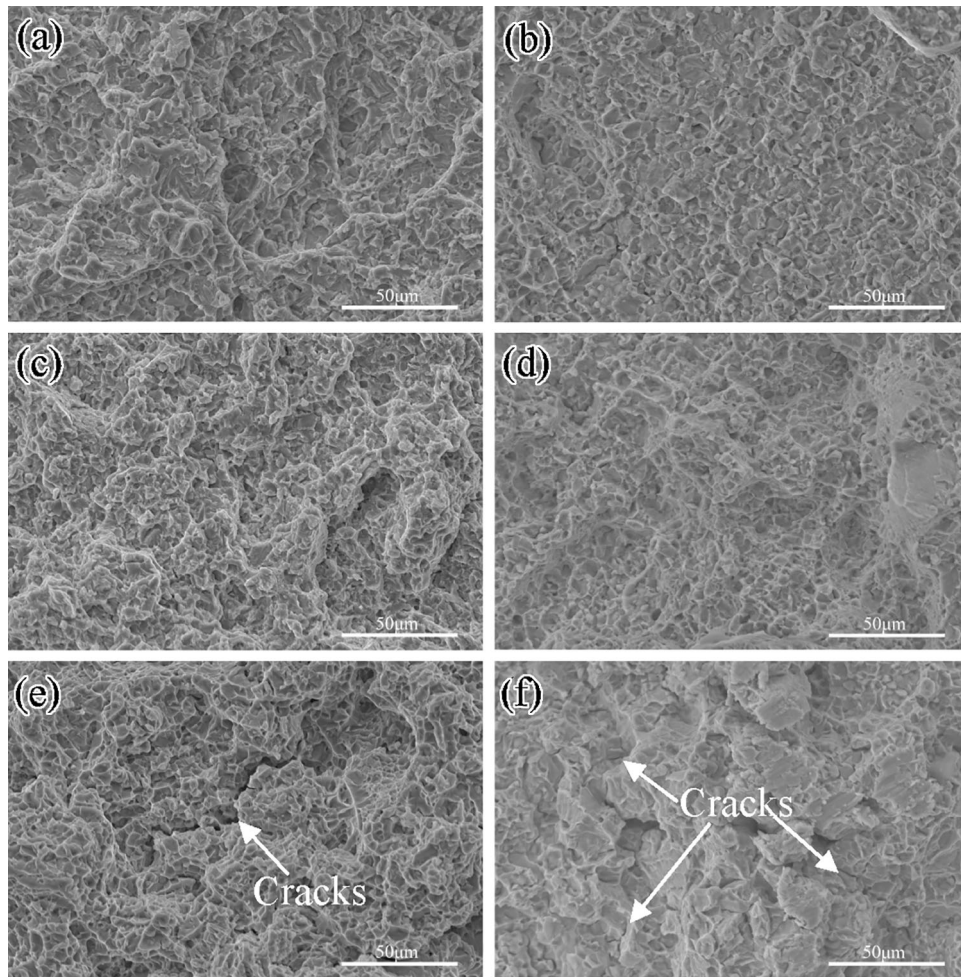
Fig. 7. Tensile fracture morphology: (a), (b) resistance furnace cooling (C1), (c), (d) vacuum furnace cooling (C3), (e), (f) water cooling (C6).
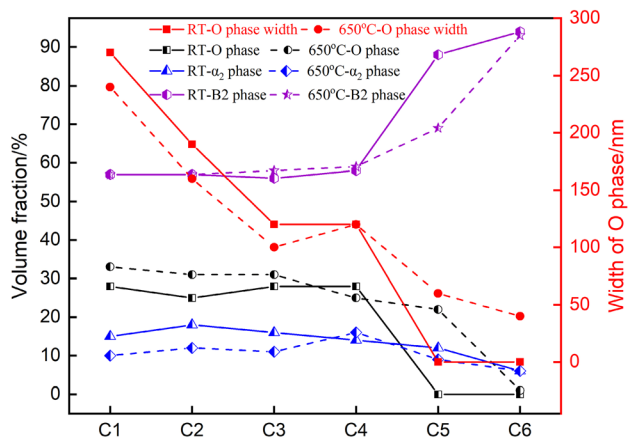

Fig. 8. Volume fraction and size of phases at RT and 650°C with different cooling rates.

with water cooling is only 1%, which is less than that of the sample with air cooling. It is possible that due to the faster cooling rate, O phase does not have enough time to grow up, resulting in a smaller size. The transition from B2 $\rightarrow$ O is very complicated and needs further study.

A severe drop in elongation was observed around 650°C for the samples with α_2 + B2 microstructure, but the phenomenon was absent in the samples with α_2 + O + B2 microstructure. This is mainly due to the existence of coarse O phase, alternating with B2 phase and α_2 phase, and coordinating deformation. In addition, due to the coarse O phase precipitation during slow cooling, the precipitation of fine O phase in B2 phase during 650°C tension is inhibited. The uncoordinated deformation of excessive B2 and fine O phase is avoided.

At RT, cracks are initiated from the prior B2 and extend along the prior B2 grain boundary. Cracks and dislocations could penetrate the grain boundaries, leading to transgranular fracture. Therefore, it has better plasticity.

At 650°C, plenty of tiny O phases are precipitated from B2 phase, and a large amount of B2/O interface is formed. In this case, the tensile specimen has a relatively flat fracture surface with fewer dimples at the fracture (Fig. 7e and f). The main reason is that dislocations accumulated in the grain boundaries and resulted in premature crack formation and failure. Some O phases are arranged along

the prior B2 grain boundary, which reduced the resistance of crack propagation along the prior B2 grain boundary.

CONCLUSION

1. With the increase of cooling rate, the room temperature tensile strength and yield strength of the alloy first increase and then decrease. When the alloy is cooled with vacuum furnace cooling (C3), the tensile strength and yield strength reach the maximum value of 1239 ± 6 MPa and 1052 ± 6 MPa, respectively. However, it has the lowest elongation of $11.2 \pm 1.6\%$. The existence of coarse O phase ensures the coordinated deformation of B2 phase and α_2 phase.
2. Compared with C1–C4, the elongation of air cooling (C5) and water cooling (C6) is $16.7 \pm 0.6\%$ and $16.5 \pm 0.5\%$, respectively. B2 phase has many slip systems, and thus it has excellent ductility, which is beneficial to improve the elongation of the alloy.
3. At 650°C, the elongation of the alloys with C5 and C6 decreases sharply, which is only $1.8 \pm 1.8\%$ and $3.7 \pm 3.1\%$. The fine O phase precipitates from B2, which reduces the resistance of crack propagation along the prior B2 grain boundary.
4. After solution treatment, the alloy is cooled at 5–10°C/min, and there are three phases of O, B2 and α_2 in the alloy, which ensure the excellent plasticity of the alloy at 650°C.

ACKNOWLEDGEMENT

CONFLICT OF INTEREST

The authors declare that they have no conflict of interest.

REFERENCES

1. D. Banerjee, A.K. Gogia, T.K. Nandi, and V.A. Joshi, *Acta Metall* 36, 871 (1988).
2. A.K. Gogia, T.K. Nandy, D. Banerjee, T. Carisey, J.L. Strudel, and J.M. Franchet, *Intermetallics* 6, 741 (1998).
3. H.Z. Zhao, B. Lu, M. Tong, and R. Yang, *Mater. Sci. Eng., A* 679, 455. https://doi.org/10.1016/j.msea.2016.10.047 (2017).
4. H.Z. Niu, Y.F. Chen, D.L. Zhang, Y.S. Zhang, J.W. Lu, W. Zhang, and P.X. Zhang, *Mater. Des.* 89, 823. https://doi.org/10.1016/j.matdes.2015.10.042 (2016).
5. Y.X. Wang, K.F. Zhang, and B.Y. Li, *Mater. Sci. Eng., A* 608, 229. https://doi.org/10.1016/j.msea.2014.04.086 (2014).
6. G.F.Wang,X.C.Sui,Q.Liu,andY.K.Liu,*Mater.Sci.Eng.,A*801, 140392.https://doi.org/10.1016/j.msea.2020.140392(2021).
7. K.H. Sim, G.F. Wang, J.M. Ju, J.L. Yang, and X. Li, *J. Alloy. Compd.* 704, 425. https://doi.org/10.1016/j.jallcom.2017.01.354 (2017).
8. J. Wu, R.P. Guo, L. Xu, Z.G. Lu, Y.Y. Cui, and R. Yang, *J. Mater. Sci. Technol.* 33, 172. https://doi.org/10.1016/j.jmst.2016.10.004 (2017).
9. M. Cheng, Z.G. Lu, J. Wu, R.P. Guo, J.W. Qiao, L. Xu, and R. Yang, *J. Mater. Sci. Technol.* 98, 177. https://doi.org/10.1016/j.jmst.2021.04.066 (2022).
10. L. Xu, R.P. Guo, J. Wu, Z.G. Lu, and R. Yang, *Acta Metall. Sin.* 54, 1537. https://doi.org/10.11900/0412.1961.2018.00360 (2018).
11. L. Xu, J. Wu, X.X. Cui, R.P. Guo, and R. Yang, *Aeronaut. Manufact. Technol.* 16, 14. https://doi.org/10.16080/j.issn1671-833x.2020.16.014 (2020).
12. C. Xue, W.D. Zeng, W. Wang, X.B. Liang, and J.W. Zhang, *Mater. Sci. Eng., A* 573, 183. https://doi.org/10.1016/j.msea.2013.03.003 (2013).
13. H.Y. Zhang, C. Li, Z.Q. Ma, L.M. Yu, H.J. Li, and Y.C. Liu, *Int. J. Miner. Metallurgy Mater.* 25, 1191. https://doi.org/10.1007/s12613-018-1671-y (2018).
14. W. Wang, W.D. Zeng, Y. Gang, D. Li, Y.P. Zheng, and X.B. Liang, *Titan. Ind. Prog.* 32, 16. https://doi.org/10.13567/j.cnki.issn1009-9964.2015.01.006 (2015).
15. I. Polozov, V. Sufiiarov, A. Kantyukov, and A. Popovich, *Intermetallics* 112, 106554. https://doi.org/10.1016/j.intermet.2019.106554 (2019).
16. Y.R. Zhang, Q. Cai, Z.Q. Ma, C. Li, L. Yu, and Y.M. Liu, *J. Alloy. Compd.* 805, 1184. https://doi.org/10.1016/j.jallcom.2019.07.149 (2019).
17. J. Wu, L. Xu, Z.G. Lu, B. Lu, Y.Y. Cui, and R. Yang, *J. Mater. Sci. Technol.* 31, 1251. https://doi.org/10.1016/j.jmst.2015.09.006 (2015).
18. X.T. Guo, W.W. Zheng, L.F. Li, and Q. Feng, *Acta Metall. Sin.* 56, 1654. https://doi.org/10.11900/0412.1961.2020.00147 (2020).
19. D. Luo, Y.Y. Cui, and R. Yang, *Mater. Sci. Forum* 475–479, 817. https://doi.org/10.4028/www.scientific.net/MSF.475-479.817 (2005).
20. H.Z. Zhao, B. Lu, and R. Yang, *Chin. J. Nonferr. Met.* 27, 708. https://doi.org/10.19476/j.ysxb.1004.0609.2017.04.005 (2017).
21. M.C. Li, Q. Cai, Y.C. Liu, Z.Q. Ma, Z.M. Wang, Y. Huang, and J.X. Yu, *Adv. Powder Technol.* 28, 1719. https://doi.org/10.1016/j.apt.2017.04.009 (2017).
22. L. Xu, R.P. Guo, C.G. Bai, J.F. Lei, and R. Yang, *J. Mater. Sci. Technol.* 30, 1289. https://doi.org/10.1016/j.jmst.2014.04.011 (2014).
23. R.P. Guo, L. Xu, B.Y. Zong, and R. Yang, *Mater. Des.* 99, 341. https://doi.org/10.1016/j.matdes.2016.02.128 (2016).
24. Z.G. Lu, J. Wu, R.P. Guo, L. Xu, and R. Yang, *Acta Metallurgica Sinica (English Letters)* 30, 621. https://doi.org/10.1007/s40195-017-0583-6 (2017).
25. J. Wu, L. Xu, B. Lu, Y.Y. Cui, and R. Yang, *Chin. J. Mater. Res.* 28, 387 (2014).
26. Z.Q. Bu, Y.G. Zhang, L. Yang, J.M. Kang, and J.F. Li, *J. Alloy. Compd.* 893, 162364. https://doi.org/10.1016/j.jallcom.2021.162364 (2022).
27. C.J. Boehlert, B.S. Majumdar, V. Seetharaman, and D.B. Miracle, *Metall. Mater. Trans. A.* 30, 2305 (1999).
28. Y. Chong, G.Y. Deng, S. Gao, J. Yi, A. Shibata, and N. Tsuji, *Scripta Mater.* 172, 77. https://doi.org/10.1016/j.scriptamat.2019.07.015 (2019).
29. W. Wang, W.D. Zeng, C. Xue, X.B. Liang, and J.W. Zhang, *Mater. Sci. Eng., A* 618, 288. https://doi.org/10.1016/j.msea.2014.09.035 (2014).
30. C.J. Boehlert, *Metall. Mater. Trans. A* 32, 1977 (2001).
31. C.J. Boehlert, and J.F. Bingert, *J. Mater. Process. Technol.* 117, 400 (2001).
32. Y. Zhang, J.Y. Liu, and J.W. Zhang, *Chin. J. Nonferr. Met.* 18, 30. https://doi.org/10.19476/j.ysxb.1004.0609.2008.01.006 (2008).
33. X.B. Liang, Y.J. Cheng, J.W. Zhang, and S.Q. Li, *Chin. J. Nonferr. Met.* 20, 611 (2010).